Applied Physics Letters

RESEARCH ARTICLE | DECEMBER 07 2022

Magnetism and microstructure of co-deposited yttrium iron garnet-barium titanate films

Tingyu Su ; Caroline A. Ross

Appl. Phys. Lett. 121, 231604 (2022)
https://doi.org/10.1063/5.0128306

Applied Physics Letters ARTICLE scitation.org/journal/apl

Magnetism and microstructure of co-deposited yttrium iron garnet-barium titanate films

Cite as: Appl. Phys. Lett. **121**, 231604 (2022); doi: 10.1063/5.0128306
Submitted: 27 September 2022 · Accepted: 25 November 2022 ·
Published Online: 7 December 2022

Tingyu Su[1] and Caroline A. Ross[2,a)]

AFFILIATIONS

[1]Department of Mechanical Engineering, Massachusetts Institute of Technology, Cambridge, Massachusetts 02139, USA
[2]Department of Materials Science and Engineering, Massachusetts Institute of Technology, Cambridge, Massachusetts 02139, USA

[a)]Author to whom correspondence should be addressed: caross@mit.edu

ABSTRACT

Yttrium iron garnet (YIG) and barium titanate (BTO) were co-deposited on (001)-orientated gadolinium gallium garnet substrates by pulsed laser deposition with composition determined by the ratio of laser shots ablating each target. With increasing shot ratios of YIG/BTO = 2.5/1, 4/1, 20/1, and 30/1, the majority phase in the film changes from textured polycrystalline perovskite to epitaxial garnet. Cross-sectional STEM characterization of the YIG-rich films reveals three distinct sublayers: the bottom layer is a coherent epitaxial garnet layer with higher unit cell volume than that of YIG; the second layer is garnet exhibiting crystalline defects and misorientation; and the upper layer is amorphous. Highly defective regions within the second layer are richer in Ba, suggesting that the microstructure is promoted by the insolubility of Ba in YIG. Temperature-dependent magnetization measurements fitted to a super-exchange dilution model indicate the presence of nonmagnetic Ti and vacancies in both octahedral and tetrahedral sites.

Magnetoelectric memory, logic, or energy devices have been proposed to take advantage of materials with both magnetic and ferroelectric properties.[1,2] However, it has been challenging to develop room temperature single phase multiferroic materials.[3] As a result, there has been intense study of two-phase materials that combine multiple functionalities, particularly epitaxial vertically aligned nanocomposites (VANs) in which two phases grow epitaxially on a substrate and are coupled at interfaces oriented normal to the film surface.[4] The most commonly studied VANs combine a ferroelectric phase, e.g., $BiFeO_3$ (BFO) and a magnetic phase, e.g., $CoFe_2O_4$ (CFO) on a perovskite substrate and exhibit magnetoelectric coupling that is mediated by elastic strain transfer.[5]

Yttrium iron garnet, or YIG ($Y_3Fe_5O_{12}$), is a ferrimagnetic oxide that is widely used in RF filters, oscillators, and magneto-optical applications as well as for spintronic devices[6] and magnonic crystals[7] due to its exceptionally low Gilbert damping. However, integration of YIG into VAN structures has proved to be challenging due to the structural incompatibility between iron garnet (lattice parameter $a_{YIG} = 1.237$ nm) and other oxides such as perovskites [e.g., $SrTiO_3$ (STO) lattice parameter $a_{STO} = 0.3905$ nm] and spinels (e.g., CFO, $a_{CFO} = 0.836$ nm). Aside from structural mismatch, mutual solubility of the phases limits nanocomposite formation. In perovskite-spinel nanocomposites, the large A-site cation of the ABO_3 perovskite has little solubility in the spinel, facilitating phase separation, but for garnet-perovskite nanocomposites, both phases can accommodate relatively large cations that occupy the dodecahedral garnet sites and the perovskite A-sites. Moreover, epitaxial growth can promote the formation of a single-phase film even when the composition differs from that of the bulk materials, impeding the growth of two-phase composites. For example, $YFeO_3$ grown on a GGG substrate forms a garnet film $Y_3(YFe_4)O_{12}$ rather than the stable $YFeO_3$ orthoferrite phase.[8]

Despite these challenges, YIG/$BaTiO_3$ (BTO) nanocomposite growth has been investigated on a perovskite substrate. Dong *et al.*[9] grew BTO pillars (~400 nm diameter) embedded in a polycrystalline YIG matrix by co-deposition of YIG and BTO on (001)-oriented STO substrates followed by annealing at 1200 °C. Jung *et al.*[10] co-deposited YIG and BTO on (001)-STO, but annealing (800—1200 °C) led to the formation of $YFeO_3$ and $BaFe_{12}O_{19}$ phases in addition to YIG and BTO. 0–3 type nanocomposites consisting of YIG crystals embedded in a BTO matrix were synthesized by Schileo *et al.*[11] using a solid-state reaction method. There have been few works on the co-deposition of YIG and BTO on a garnet substrate, nor the successful preparation of epitaxial garnet VANs.

Here, we investigate whether two-phase YIG-BTO nanocomposites can be grown directly on $Gd_3Ga_5O_{12}$ (GGG) garnet substrates by pulsed laser deposition (PLD). We find that textured perovskite films

grow for high BTO content whereas epitaxial garnet films grow for high YIG content. Films with a high YIG content consist of a strained garnet matrix with inverted conical polycrystalline regions enriched with Ba, and the films became amorphous as the thickness increased. The Curie temperature of the high YIG content films is smaller than that of bulk YIG, and the temperature dependence of the magnetization was fitted to reveal the site occupancy of the octahedral and tetrahedral sites of the Ba, Ti-containing garnet.

Films were co-deposited by combinatorial PLD[12] on (001)-oriented GGG substrates by alternating ablation of two stoichiometric targets, YIG and BTO, with different ratios of laser shots: 2.5/1, 4/1, 20/1, and 30/1. The laser was operated at 248 nm wavelength with a repetition rate of 2 Hz and fluence at the target ~2.5 J/cm^2. During growth, the O_2 partial pressure was kept at 150 mTorr, and the temperature of the substrate heater was set to 900 °C with the actual temperature of the substrate around 150 °C lower. The samples are named according to their shot ratios, e.g., YB2.5 has a shot ratio of YIG/BTO = 2.5/1. The growth rate of YIG on GGG is 1.5 nm/1000 shots and that of BTO on STO is 17.5 nm/1000 shots, i.e., BTO deposited about ten times faster than YIG (see the supplementary material). Wavelength dispersive x-ray spectroscopy (WDS, JEOL JXA-8200 Superprobe, Table I) yields molar compositions, which are consistent with the much higher deposition rate of BTO. High resolution x-ray diffraction (HRXRD) and x-ray reflectivity (XRR) measurements were performed on a Rigaku Smartlab diffractometer with Cu $K_{\alpha 1}$ radiation ($\lambda = 1.5406$ Å). Cross-sectional scanning transmission electron microscopy (STEM) was performed using a Titan Themis Z aberration-corrected STEM with accelerating voltage of 300 kV and 200 kV on lamella samples prepared using a Raith VELION FIB-SEM system with Au^+ source. Electron diffraction patterns were taken in a microprobe mode using a Ceta camera. Magnetic hysteresis loops at different temperatures were measured using a Quantum Design MPMS3 superconducting quantum interference device (SQUID) magnetometer (15–400 K) and a vibrating sample magnetometer with an oven (373–500 K) in fields up to 500 Oe, subtracting background signals using a linear fit. The maximum field was chosen to be sufficient to saturate the sample in plane but small enough to avoid nonlinearities in the GGG substrate signal. The surface topography was characterized using a Cypher S atomic force microscope (AFM) in the tapping mode.

The x-ray diffraction ($2\theta = 15°$–$80°$) measurements of YIG:BTO are shown in Fig. 1(a). At a lower YIG content (YB2.5, YB4), the most intense peaks come from perovskite (*hh*0) and (00 *l*), consistent with the rectangle-on-cube or cube-on-cube growth of BTO/garnet discussed by Ruf *et al.*[13] and no garnet peak is detectable other than that of the substrate. The BTO perovskite structure can accommodate Y and Fe, i.e., $(Y_zBa_{1-z})(Fe_zTi_{1-z})O_3$ has full solid solubility,[14,15] explaining the formation of a single phase perovskite film at a high BTO content. Grazing incidence x-ray diffraction (GIXRD) confirms the textured perovskite growth, and VSM measurements (see the supplementary material) indicate that the films are non-magnetic. The surface topography measured by AFM is shown in Figs. 1(b1)–1(b2): the YB2.5 and YB4 perovskite surfaces have an r.m.s. surface roughness of order 3–4 nm (Table I).

Here, we focus on analysis of the high YIG content films (YB20, YB30) due to their magnetic properties. YB20 exhibits prominent ~100 nm diameter surface features of ~10 nm height, and YB30 has sparser features of similar height, Figs. 1(b3)–1(b4). XRD shows only epitaxial garnet peaks with an out-of-plane lattice expansion compared to the lattice of GGG. The surface roughness and structural disorder (see below) account for the lack of Laue fringes around the x-ray peaks, which are seen in other garnet films with a range of substituents (e.g., Tm, Ce, Y, etc.).[8,16,17]

Sample YB30 [Fig. 1(b4)] was analyzed to determine the structure and composition of the matrix and surface features. The HADDF and bright field images of a region of the film (without surface features) along the [001] zone axis are given in Figs. 2(a) and 2(b), respectively. The film is composed of three layers: a coherent layer of garnet of around 10 nm thickness at the substrate/film interface, a columnar crystalline garnet layer of ~55 nm thickness showing strain and dislocations, and an amorphous layer of ~15 nm thickness at the top. A higher magnification view of the interface between the substrate and coherent layers is shown in Fig. 2(e), confirming coherent epitaxial crystal growth at the early stage of film growth. As a comparison, one of the column boundaries is shown in Fig. 2(d), revealing a dislocation that nucleated 8 nm above the interface.

The interface between the amorphous and columnar regions is shown in Fig. 2(c), and the electron diffraction patterns of the two regions are shown in Figs. 2(f) and 2(g). The thickness of this sample measured by XRR (shown in the supplementary material) is 81 nm, which is in good agreement with the STEM measurement, including both the crystalline and amorphous regions [Figs. 2(a) and 2(b)]. In the elemental maps of Fig. 2(h), Y, Fe, Ba/Ti, and O are presented throughout the film but the Ba and Ti peaks overlap and the elements cannot be analyzed independently.

For the YB30 sample, the critical thickness for defect formation h_{def} is 10 nm, and the critical thickness for the crystal-to-amorphous transition h_{am} is 66 nm (Table I). The crystal-to-amorphous transition also happened for the YB20 sample, as shown in Fig. 3, but with $h_{def} = 5$ and $h_{am} = 10$ nm, and the amorphous region was 20 nm thick. We attribute the origin of the amorphous layer to the increasing

TABLE I. Summary of composition, structure, and thickness of YIG/BTO samples. t_{film} is the film thickness, h_{def} is the thickness at which defects nucleate, and h_{am} is the thickness at which the film becomes amorphous. The composition and volume ratio are based on WDS quantification and the densities of YIG (5.11 g/cm^3) and BTO (6.02 g/cm^3).

Sample	Shots ratio YIG/BTO	Molar composition $Y_3Fe_5O_{12}/BaTiO_3$	t_{film} (nm)	h_{def} (nm)	h_{am} (nm)	Volume YIG/BTO	Structure	RMS roughness nm
YB2.5	2.5:1	0.17	···	···	···	0.63	Textured perovskite	4.3
YB4	4:1	0.27	···	···	···	1.01	Textured perovskite	3.3
YB20	20:1	1.33	35	5	10	4.96	Epitaxial garnet	2.5
YB30	30:1	1.97	81	10	66	7.34	Epitaxial garnet	2.5

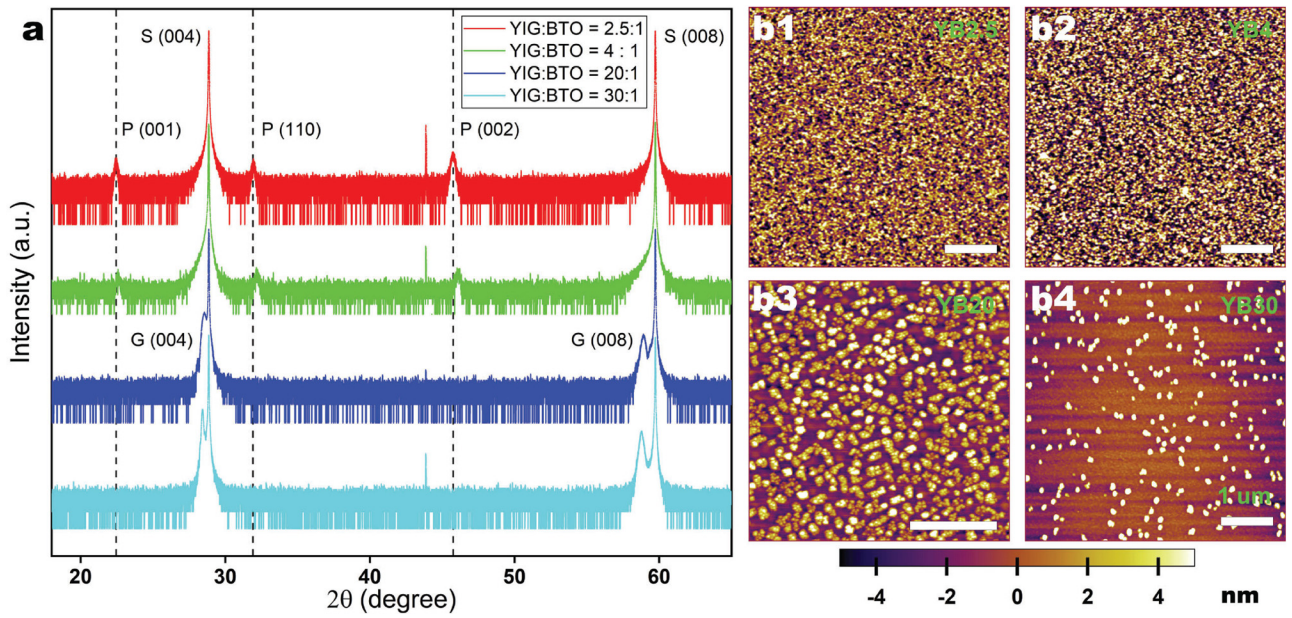

FIG. 1. X-ray diffraction and surface topography. (a) HRXRD of co-deposited YIG/BTO samples with different shot ratios. (b) AFM height images: (b1)–(b4) correspond to YIG/BTO = 2.5/1, 4/1, 20/1, and 30/1, scale bar = 1 μm, and the color bar represents height in nm.

roughness caused by the strain or surface evolution in the manner of the breakdown in epitaxial growth of Si or Ge reported in Refs. 18–20. The onset of defects and amorphization in YB20 at lower thicknesses correlates with the higher content of BTO. The amorphous layer is expected to be paramagnetic (similar to amorphous iron oxide[21]) and not to contribute to the magnetic hysteresis; therefore, the effective film thickness of YB30 is taken as 66 nm for our subsequent magnetic analysis.

The HADDF cross-sectional image through one of the surface protrusions in YB30 [Fig. 1(b4)] is presented in Fig. 4(a), indicating that the surface feature is associated with an inverted cone whose apex originates ~10 nm (i.e., at ~h_{def}) above the substrate film interface. Figure 4(c) shows a higher magnification of the region marked by the red box, and larger images are given in the supplementary material. The electron diffraction patterns of the substrate below the cone apex and the blue circle and red circle regions are shown in Figs. 4(a2), 4(a1), and 4(a3), respectively, confirming changes in the crystal orientation and/or structure in the cone region. The small size of the crystallites in the cone region limits the identification of the crystal structure, but some of the crystallites in Fig. 4(c) appear to be garnet of different orientations vs the matrix. The elemental mapping is shown in Figs. 4(b1)–4(b5). The matrix consists primarily of Y, Fe, and O, while the cone region has similar O content but less Fe than the matrix. Ba is present throughout the film but is concentrated in the cone regions, where Ba and Y are distributed in complementary locations. We present another example of an inverted cone in the supplementary material, which has the wider cone angle but similar elemental distributions.

Based on the measured out-of-plane lattice parameter of 1.255 nm and in-plane coherency [Fig. 2(e)], the unit cell volume of the Ba,Ti-YIG is 1.5% larger than that of GGG. The large Ba^{2+} ion (radius ~1.61 Å, for coordination number CN = 12)[22] has a solubility of less than 0.01% in bulk YIG,[23] though the chemical mapping and the WDS suggest a larger concentration in the film. Ti^{4+} (radius ~0.74 Å, CN = 8),[22] which is smaller than Fe^{3+} (radius ~0.78 Å, CN = 8)[22] it replaces, can be incorporated up to 15% in YIG.[24,25] Co-substitution of Ba^{2+}:Ti^{4+} in a ratio of 1:1 leads to charge balance, whereas incorporation of more Ti than Ba could be accommodated via vacancies on the Fe sites, divalent Fe or trivalent Ti in Ba,Ti-YIG.

The cation substitution into YIG can be probed through its effect on the ferrimagnetism of the film. In-plane magnetic hysteresis loops with fields up to 500 Oe at different temperatures are presented in Fig. 5(a), after a linear subtraction to exclude the substrate paramagnetic signal. With increasing temperature from 35 to 400 K, the coercivity is reduced from 75 to 5 Oe, and the saturation magnetization (M_s) drops from 220 to 60 emu cm^{-3}. The Ms(T) data are presented in Fig. 5(b), in which the shift between VSM and SQUID data is attributed to offset between the temperature sensors.

Dionne's super-exchange dilution model[26] is used to quantitatively explore the substitutional site preference. The molecular field coefficient fitting is conducted as described in our previous work,[8] treating the epitaxial and crystalline regions of the film as having the same magnetization. We rewrite the YIG chemical formula as $\{Y_{3\cdot(1-kc)}X_{3\cdot kc}\}[Fe_{2\cdot(1-ka)}X_{2\cdot ka}]\ (Fe_{3\cdot(1-kd)}X_{3\cdot kd})O_{12}$, where k_a, k_d, and k_c stand for the fractional substitution in the a (octahedral), d (tetrahedral), and c (decahedral) sites, respectively, and X represents nonmagnetic species such as Ba^{2+}, Ti^{4+}, or vacancies, V. Since dodecahedral species Y and X are non-magnetic, the net magnetization is independent of k_c and the fitting is only done for k_a and k_d.

The fitting of experimental data and Dionne's model by the MATLAB non-linear least squares method gives $k_a = 0.2135$ and $k_d = 0.0737$ together with Curie temperature $T_c = 460$ K [Fig. 5(b)]. Based on a steric argument,[27] we assume any Ba^{2+} present would

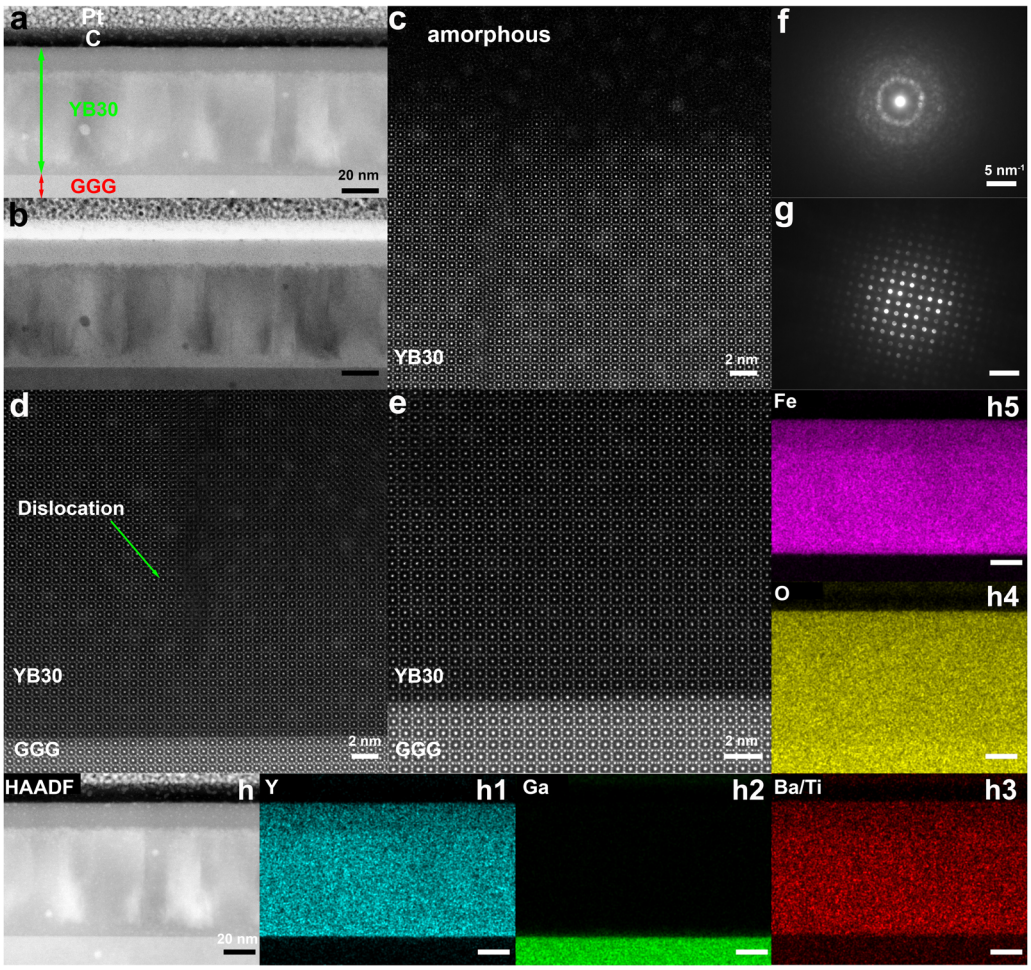

FIG. 2. STEM cross-sectional view of the YIG/BTO = 30/1 sample in the region without protrusions. (a) HADDF and (b) bright field images, scale bar = 20 nm. Zoomed view of interface between the substrate and film with dislocation (d) and without dislocation (e) and interface between crystalline and amorphous regions (c), scale bar = 2 nm. Electron diffraction pattern in the microprobe mode of amorphous (f) and crystalline regions (g), scale bar = 5 nm^{-1}. EDS mapping: scale bar = 20 nm.

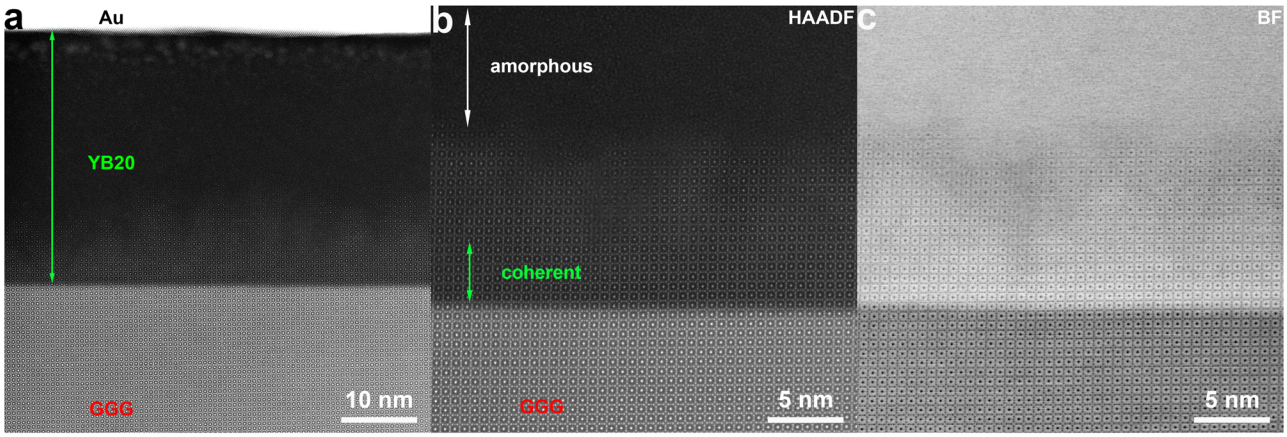

FIG. 3. STEM cross-sectional view of the YIG/BTO = 20/1 sample. (a) HAADF scale bar = 10 nm. (The top bright layer is the Au protection layer.) HADDF (b) and bright field (c) at higher magnification, scale bar = 5 nm.

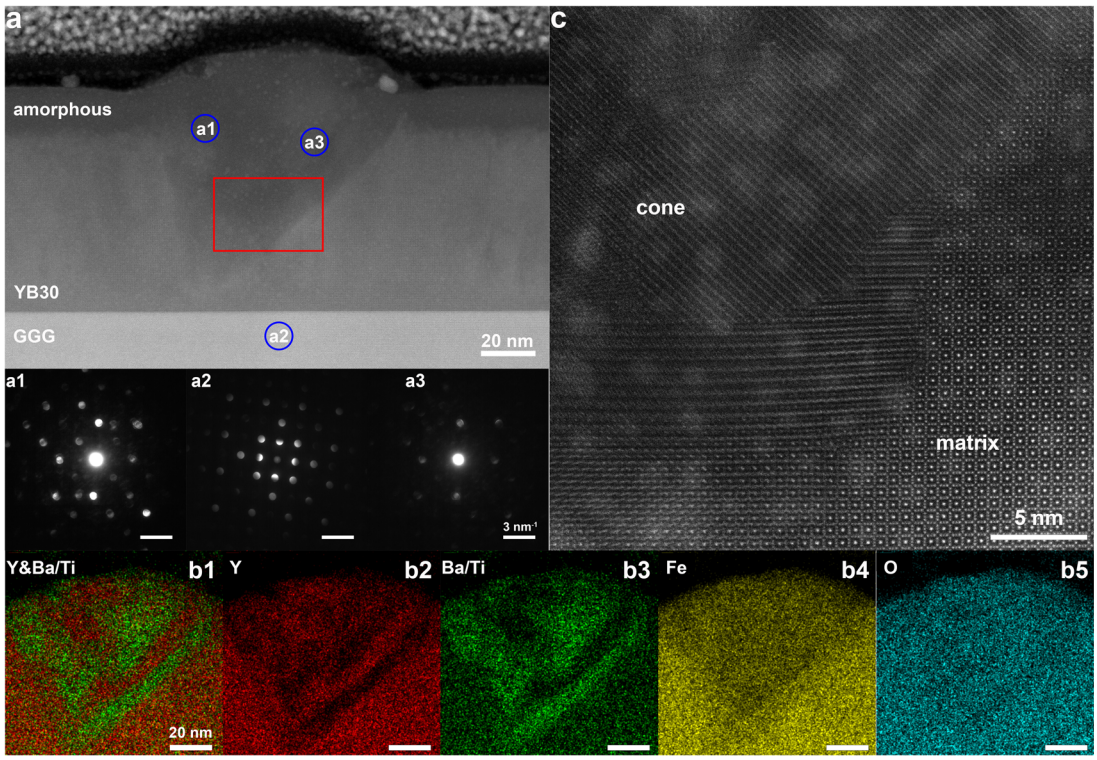

FIG. 4. (a) STEM cross-sectional view of the YIG/BTO = 30/1 sample on the "bump" region. Electron diffraction patterns of the substrate below the cone (a2), blue region (a1), and red region (a3), scale bar = 3 nm^{-1}. Zoomed region of red square area (c), scale bar = 5 nm. EDS mapping of the cone region (b1)–(b5), scale bar = 20 nm.

preferentially occupy the c sites and Ti^{4+} preferentially occupies a and d sites. Assuming that the Y:Fe ratio remains at 3:5, $3k_c = 0.39$ and the fitted composition becomes $Y_{2.61}(Ba,Ti)_{0.39}Fe_{4.35}(Ti,V)_{0.65}O_{12}$, neglecting other ionic species such as non-trivalent Fe or vacancies on the oxygen or c sites. Geller[24,25] and Espinosa[28] found that for the single phase polycrystalline $\{Y_{3-x}Ca_x\}Fe_{5-x}Ti_xO_{12}$ ($x < 0.65$), 30% of Ti occupies the tetrahedral site, which is in consistent with our fitting: tetrahedral/total Ti occupancy = $(3k_d)/(3k_d+2k_a) = 0.34$. Furthermore,

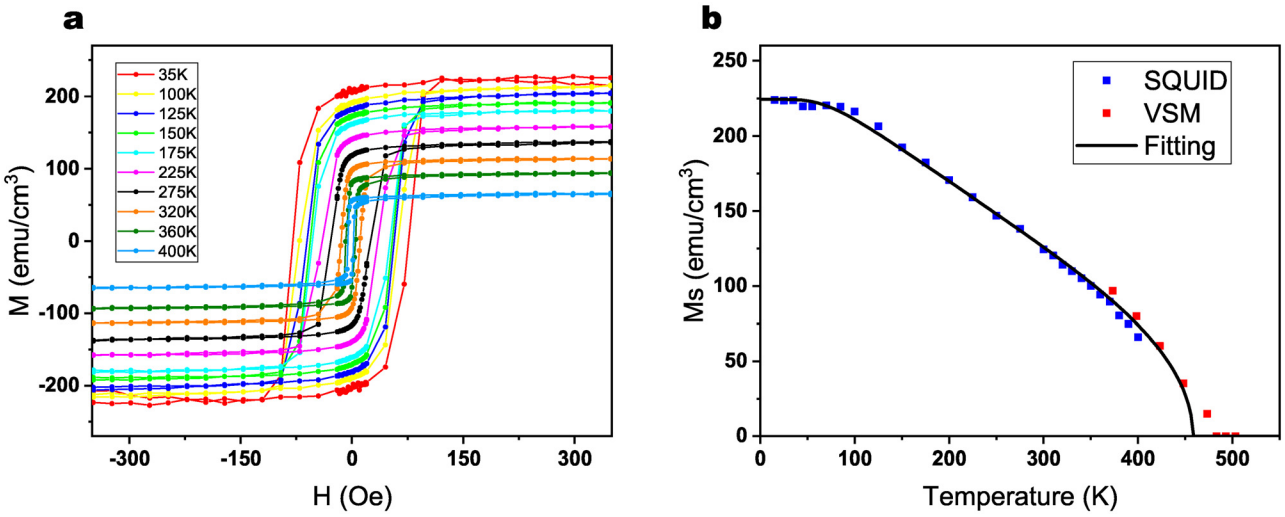

FIG. 5. Magnetic properties of the YIG/BTO = 30/1 sample. (a) In-plane hysteresis loop taken at different temperatures using SQUID by subtracting the linear background GGG signal. (b) Temperature-dependence of saturation magnetization (Ms) and molecular field theory fitting result.

the Curie temperature of $\{Y_{2.4}Ca_{0.6}\}Fe_{4.4}Ti_{0.6}O_{12}$ was reported as 444 K, which is similar to our result $T_c = 460$ K.

The nominal molar composition of YB30 based on the quantification from WDS is YIG:BTO = 1.97:1 = 1:0.5 (Table I). From the magnetic data, the c, a, and d-site substitution of 1.04 represents an upper bound for the Ba+Ti+V content. If we assume all Ba and Ti participate in substitution, then the molar ratio of YIG:(BTO+V/2) = (2.61/3):0.52 = 1:0.6, which compared to the measured ratio of YIG:BTO = 1:0.5 implies the presence of vacancies. Vacancies may be promoted by crystal distortion due to the Ba^{2+} substitution. The super-exchange dilution model neglects the contribution of the inverted conical regions, which might affect the estimation of the vacancy content.

Due to the negligible Ba^{2+} solubility in bulk YIG, we do not expect Ba^{2+} to be accommodated at the same concentration as Ti^{4+}. However, the large unit cell expansion of Ba,TiYIG does support the presence of more Ba than the bulk solubility limit. Charge-balance of Ti^{4+} may be accomplished by cation vacancies or non-trivalent Fe.

To summarize, a series of films with varying YIG:BTO ratios was grown on GGG substrates. The high-BTO content films formed a polycrystalline textured perovskite, which is consistent with the high solubility of Y and Fe in BTO, and the cube-on-cube or rectangle-on-cube epitaxy reported for BTO grown on garnet.[13] In contrast, in the YIG-rich regime, the garnet substrate epitaxially stabilized a garnet phase of Ba,Ti-YIG. The substituted YIG has a larger unit cell compared to bulk YIG, which is attributed to the incorporation of large Ba ions, and the film grows with in-plane compressive strain, which is relieved above a certain thickness h_{def} by formation of dislocations and nucleation of misoriented crystals, which form inverted-conical regions. As the film becomes thicker and rougher, eventually epitaxy breaks down at thickness h_{am}, and an amorphous oxide layer is formed. The presence of defects, the nanocrystalline conical regions, and amorphization differs from other reports of strained garnet films[16,17,29] and suggests that the substituents, particularly Ba, may lower the barrier to form misfit dislocations or other defects in addition to the lattice expansion effect. The presence of non-magnetic substituents on the Fe sites (i.e., Ti and vacancies) is evident from the M(T) behavior.

Excess Ba is believed to be concentrated into inverted conical regions that nucleate at the same thickness as the misfit dislocations grow laterally. Unlike VANs, these regions are inhomogeneous and consist of multiple crystals with different orientations. The formation of YIG:BTO VANs, therefore, appears to be impeded by the mutual solubility of the cations and by the lack of a lattice match that would promote epitaxy between the two phases. Unlike in BFO/CFO, where Bi is insoluble in the spinel, the large ions (Y and Ba) can distribute between the two phases (though the solubility of Ba in YIG is limited), as can Fe and Ti. On a GGG substrate, formation of substituted YIG is favored and the strain caused by the incorporated Ba promotes defects and structural inhomogeneities. These results demonstrate the compositional dependence of the structure and magnetic properties of thin-film YIG and provide guidance in the selection of oxide materials for synthesis of multiphase thin films.

See the supplementary material for details of WDS quantification, STEM images, XRR fitting and super-exchange dilution model code.

The authors gratefully acknowledge the support from NSF via Award No. DMR 1911792 and the use of MRSEC shared facilities under No. DMR 1419807. This work was performed in part on the Raith VELION FIB-SEM and Titan Themis Z STEM at the MIT Nano Characterization Facilities (Award No. DMR-2117609). The authors thank Dr. Frances Ross for inspiration, Dr. Aubrey Penn for acquisition of STEM images, and Dr. Yang Yu for Raith VELION FIB training.

AUTHOR DECLARATIONS

Conflict of Interest

The authors have no conflicts to disclose.

Author Contributions

Tingyu Su: Conceptualization (equal); Data curation (equal); Formal analysis (equal); Software (equal); Visualization (equal); Writing – original draft (equal); Writing – review & editing (equal). **Caroline A. Ross:** Funding acquisition (equal); Project administration (equal); Supervision (equal); Writing – review & editing (equal).

DATA AVAILABILITY

The data that support the findings of this study are available from the corresponding author upon reasonable request.

REFERENCES

[1]A. Nicolenco, M. de h-Óra, C. Yun, J. MacManus-Driscoll, and J. Sort, "Strain-gradient effects in nanoscale-engineered magnetoelectric materials," APL Mater. **9**(2), 020903 (2021).
[2]A. Chen and Q. Jia, "A pathway to desired functionalities in vertically aligned nanocomposites and related architectures," MRS Bull. **46**(2), 115–122 (2021).
[3]N. A. Hill and A. Filippetti, "Why are there any magnetic ferroelectrics?," J. Magn. Magn. Mater. **242–245**, 976–979 (2002).
[4]H. Zheng, J. Wang, S. E. Lofland, Z. Ma, L. Mohaddes-Ardabili, T. Zhao *et al.*, "Multiferroic $BaTiO_3$-$CoFe_2O_4$ nanostructures," Science **303**(5658), 661–663 (2004).
[5]J. T. Heron, M. Trassin, K. Ashraf, M. Gajek, Q. He, S. Y. Yang *et al.*, "Electric-field-induced magnetization reversal in a ferromagnet-multiferroic heterostructure," Phys. Rev. Lett. **107**(21), 217202 (2011).
[6]A. V. Chumak, V. I. Vasyuchka, A. A. Serga, and B. Hillebrands, "Magnon spintronics," Nat. Phys. **11**(6), 453–461 (2015).
[7]H. Qin, G. J. Both, S. J. Hämäläinen, L. Yao, and S. van Dijken, "Low-loss YIG-based magnonic crystals with large tunable bandgaps," Nat. Commun. **9**(1), 5445 (2018).
[8]T. Su, S. Ning, E. Cho, and C. A. Ross, "Magnetism and site occupancy in epitaxial Y-rich yttrium iron garnet films," Phys. Rev. Mater. **5**(9), 094403 (2021).
[9]G. Dong, Z. Zhou, X. Xue, Y. Zhang, B. Peng, M. Guan *et al.*, "Ferroelectric phase transition induced a large FMR tuning in self-assembled $BaTiO_3$:$Y_3Fe_5O_{12}$ multiferroic composites," ACS Appl. Mater. Interfaces **9**(36), 30733–30740 (2017).
[10]H. K. Jung, J. H. Mun, H. J. Lee, J. M. Song, and D. H. Kim, "Magnetic property modulation in sputter-grown $BaTiO_3$–$Y_3Fe_5O_{12}$ composite films," Ceram. Int. **47**(5), 7062–7068 (2021).
[11]G. Schileo, C. Pascual-Gonzalez, M. Alguero, I. M. Reaney, P. Postolache, L. Mitoseriu *et al.*, "Yttrium iron garnet/barium titanate multiferroic composites," J. Am. Ceram. Soc. **99**(5), 1609–1614 (2016).
[12]N. M. Aimon, D. H. Kim, H. Y. Choi, and C. A. Ross, "Deposition of epitaxial $BiFeO_3$/$CoFe_2O_4$ nanocomposites on (001) $SrTiO_3$ by combinatorial pulsed laser deposition," Appl. Phys Lett. **100**(9), 092901 (2012).
[13]T. Ruf, S. Merker, F. Syrowatka, P. Trempler, G. Schmidt, M. Lorenz *et al.*, "Preferential growth of perovskite $BaTiO_3$ thin films on $Gd_3Ga_5O_{12}$(100) and $Y_3Fe_5O_{12}$(100) oriented substrates by pulsed laser deposition," Mater. Adv. **3**(12), 4920–4931 (2022).

[14]M. Afqir, M. Elaatmani, A. Zegzouti, A. Oufakir, and M. Daoud, "Sol–gel synthesis, structural and dielectric properties of Y-doped $BaTiO_3$ ceramics," J. Mater. Sci. **30**(6), 5495–5502 (2019).
[15]F. Lin, D. Jiang, X. Ma, and W. Shi, "Influence of doping concentration on room-temperature ferromagnetism for Fe-doped $BaTiO_3$ ceramics," J. Magn. Magn. Mater. **320**(5), 691–694 (2008).
[16]E. R. Rosenberg, K. Litzius, J. M. Shaw, G. A. Riley, G. S. D. Beach, H. T. Nembach *et al.*, "Magnetic properties and growth-induced anisotropy in yttrium thulium iron garnet thin films," Adv. Electron. Mater. **7**(10), 2100452 (2021).
[17]A. Kehlberger, K. Richter, M. C. Onbasli, G. Jakob, D. H. Kim, T. Goto *et al.*, "Enhanced magneto-optic Kerr effect and magnetic properties of $CeY_2Fe_5O_{12}$ epitaxial thin films," Phys. Rev. Appl. **4**(1), 014008 (2015).
[18]O. Gurdal, P. Desjardins, J. R. A. Carlsson, N. Taylor, H. H. Radamson, J. E. Sundgren *et al.*, "Low-temperature growth and critical epitaxial thicknesses of fully strained metastable $Ge_{1-x}Sn_x$ ($x \lesssim 0.26$) alloys on Ge(001)2×1," J. Appl. Phys. **83**(1), 162–170 (1998).
[19]D. J. Eaglesham, H. J. Gossmann, and M. Cerullo, "Limiting thickness h_{epi} for epitaxial growth and room-temperature Si growth on Si(100)," Phys. Rev. Lett. **65**(10), 1227–1230 (1990).
[20]K. A. Bratland, Y. L. Foo, J. A. N. T. Soares, T. Spila, P. Desjardins, and J. E. Greene, "Mechanism for epitaxial breakdown during low-temperature Ge(001) molecular beam epitaxy," Phys Rev B **67**(12), 125322 (2003).
[21]L. Machala, R. Zboril, and A. Gedanken, "Amorphous iron(III) oxide—A review," J. Phys. Chem. B **111**, 4003–4018 (2007).
[22]R. D. Shannon, "Revised effective ionic radii and systematic studies of interatomic distances in halides and chalcogenides SO," Acta Crystallogr., Sect. A **32**(5), 751–767 (1976).
[23]I. D. Lomako and A. G. Dutov, "Effect of nonstoichiometry and technological impurities on the structural properties and absorption of $Y_3Fe_5O_{12}$ crystals in the IR range," Kristallografiya **47**(1), 120–123 (2002).
[24]S. Geller, R. C. Sherwood, G. P. Espinosa, and H. J. Williams, "Substitution of Ti^{4+}, Cr^{3+}, and Ru^{4+} ions in yttrium iron garnet," J. Appl. Phys. **36**(1), 321 (1965).
[25]S. Geller, H. J. Williams, G. P. Espinosa, and R. C. Sherwood, "Importance of intrasublattice magnetic interactions and of substitutional ion type in the behavior of substituted yttrium iron garnets," Bell Syst. Tech. J. **43**(2), 565–623 (1964).
[26]G. F. Dionne, "Molecular field coefficients of substituted yttrium iron garnets," J. Appl. Phys. **41**(12), 4874–4881 (1970).
[27]M. A. Gilleo and S. Geller, "Substitution for iron in ferrimagnetic yttrium-iron garnet," J. Appl. Phys. **29**(3), 380–381 (1958).
[28]G. P. Espinosa, "A crystal chemical study of titanium (IV) and chromium (III) substituted yttrium iron and gallium garnets," Inorg. Chem. **3**(6), 848–850 (1964).
[29]L. Soumah, N. Beaulieu, L. Qassym, C. Carrétéro, E. Jacquet, R. Lebourgeois *et al.*, "Ultra-low damping insulating magnetic thin films get perpendicular," Nat. Commun. **9**(1), 3355 (2018).